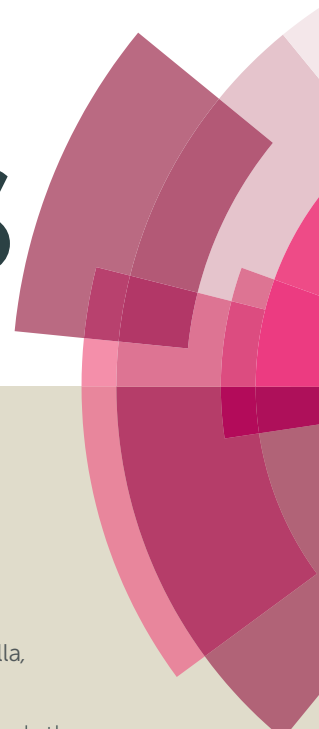


RSC Advances



This article can be cited before page numbers have been issued, to do this please use: G. F. Leal, S. F. Moya, D. M. Meira, D. H. Barrett, E. Teixeira Neto, A. A. D. S. Curvelo, V. Teixeira da Silva and C. B. Rodella, *RSC Adv.*, 2016, DOI: 10.1039/C6RA15819F.



This is an *Accepted Manuscript*, which has been through the Royal Society of Chemistry peer review process and has been accepted for publication.

Accepted Manuscripts are published online shortly after acceptance, before technical editing, formatting and proof reading. Using this free service, authors can make their results available to the community, in citable form, before we publish the edited article. This *Accepted Manuscript* will be replaced by the edited, formatted and paginated article as soon as this is available.

You can find more information about *Accepted Manuscripts* in the [Information for Authors](#).

Please note that technical editing may introduce minor changes to the text and/or graphics, which may alter content. The journal's standard [Terms & Conditions](#) and the [Ethical guidelines](#) still apply. In no event shall the Royal Society of Chemistry be held responsible for any errors or omissions in this *Accepted Manuscript* or any consequences arising from the use of any information it contains.

Promotion effects of Pd on tungsten carbide catalysts: physiochemical properties and cellulose conversion performance

Glauco F. Leal^{a,b}, Silvia F. Moya^a, Debora M. Meira^{a,c}, Dean H. Barrett^a, Erico Teixeira-Neto^d, Antonio Aprígio S. Curvelo^{b,e}, Victor Teixeira da Silva^f and Cristiane B. Rodella^a

^a *Brazilian Center for Research in Energy and Materials (CNPEM) - Brazilian Synchrotron Light Laboratory (LNLS), C. P. 6192, 13083-970, Campinas, SP, Brazil*

^b *Institute of Chemistry of São Carlos (IQSC)/University of São Paulo (USP)/ C.P. 780, CEP 13560-970, São Carlos, SP, Brazil*

^c *European Synchrotron Radiation Facility (ESRF), 71 Avenue des Martyrs, 38000 Grenoble, France*

^d *CNPEM – Brazilian Nanotechnology National Laboratory (LNNano)-CNPEM, CP 6192, CEP 13083-970, Campinas, SP, Brasil*

^e *CNPEM - Brazilian Bioethanol Science and Technology Laboratory (CTBE), C. P. 6192, 13083-970, Campinas, SP, Brazil*

^f *Universidade Federal do Rio de Janeiro/COPPE/Chemical Engineering Program/NUCAT, P.O. Box 68502, Rio de Janeiro, RJ 21945-970, Brazil*

Abstract

A multi-functional catalyst, which is able to perform both retro-aldol reactions followed by hydrogenation, is required to convert cellulose into the value-added ethylene glycol (EG) in a one-pot reaction. Herein, we show results of a catalyst comprising Pd-promoted tungsten carbide supported on activated carbon. Pd acts to hinder carbon deposition onto the catalyst surface during the carburization process, through the inhibition of methane decomposition species on the catalyst surface. XPS and TEM analysis show a cleaner surface which improves the W/C ratio. The enhanced interaction between Pd and W₂C, result in higher cellulose conversions, and higher ethylene glycol (EG) yields when compared to non-promoted or Ni promoted tungsten carbide catalysts reported elsewhere. XAS, HR-TEM and SI-XEDS analysis showed Pd nanoparticles are well dispersed on the surface and in contact with W₂C. Despite higher carburization temperatures, Pd-promoted tungsten

carbide catalysts enhance the catalytic properties of the one-pot cellulose conversion reaction towards EG production when compared to Ni-promoted catalysts under the same catalytic reaction conditions.

Introduction

Heterogeneous catalysts have been at the forefront of the chemical industry for over two centuries. These catalysts are now making an impact on the new emerging economy based on biomass conversion to produce bio-fuels and chemicals¹⁻⁹. Cellulose is the most abundant form of biomass and a key substrate in catalytic reactions and chemical processes that provide bio-based products^{2,5,6,8-10}. In the past 15 years, significant advances have been made in developing and understanding the correlation between cellulose processing and catalyst properties towards an efficient, profitable and environmentally friendly production of chemicals^{2,8-12}. Tungsten carbide catalysts supported on activated carbon have been shown to be a potential catalyst for low-cost and sustainable ethylene glycol (EG) production in one-pot cellulose conversion reactions. Many papers deal with cellulose transformation pathways using complex and multi-functional Ni-promoted tungsten carbide catalysts¹³⁻¹⁹. However, only a few give insights into the structural, electronic and surface properties of these catalysts from catalyst preparation to the reaction steps. Our previous work²⁰, focused on the physical and chemical effects of Ni on tungsten carbide catalysts and revealed direct correlations between the metal promoter performance and the carburization process. The work showed an improvement in the Ni/W₂C/C interaction which improved selectivity towards ethylene glycol. The highly dispersed Ni improved properties such as hydrogen spillover, lower carburization temperature and improved ability to perform retro-aldol reactions. The drawback however, was enhanced methane decomposition which deposits carbon on the catalyst surface and lowers the catalysts ability to convert cellulose.

Although noble metals are more costly than base metals they provide exceptional hydrogenation and retro-aldol properties in catalytic reactions involving biomass^{2,10,12,21-25}. Moreover, noble metals are less thermodynamically and kinetically active towards CH_x (1 ≤ x ≤ 4) decomposition when compared to Ni²⁶⁻²⁹. This characteristic is important in controlling carbon deposition during the carburization step during the catalyst synthesis.

The use of a noble metal as a tungsten carbide promoter may offer a profitable balance amongst catalyst cost, physical and chemical properties and catalytic activity to obtain high value-added platform chemicals from cellulose. Thus, we turned our attention to the much less explored promoter Pd³⁰. Herein, our research strategy was to perform *in situ* X-ray diffraction (XRD), X-ray absorption spectroscopy (XAS) and mass spectroscopy analysis during the carburization processes as well as X-ray Photoelectron Spectroscopy (XPS), N₂ Physisorption, High Resolution Transmission Electron Microscopy (HR-TEM) and X-Ray Energy Dispersive Spectrum Imaging (SI-XEDS) to provide a comprehensive insight into the structural, electronic and surface properties of the Pd-promoted tungsten carbide supported on activated carbon catalysts. In addition, the catalytic behavior was substantially investigated in one-pot cellulose conversion reactions for ethylene glycol production.

Experimental

Catalyst Preparation

Tungsten and palladium impregnation on activated carbon was performed using a method previously reported²⁰. The Pd precursor (PdCl₂ – Sigma-Aldrich) was dissolved in hot HCl (60°C) under magnetic stirring due to the low solubility of PdCl₂. The solution was then evaporated and water was added and stirred for 5 min followed by evaporation to remove the excess HCl. The final aqueous solution was prepared at room temperature and impregnated into the W/C sample to obtain 1 and 2 wt.% Pd in the final composition.

The carburization process was carried out under a total flow of 100 mL.min⁻¹ using a mixture of CH₄ (10% v/v) and H₂ (90% v/v) from room temperature to 850°C at a rate of 8°C min⁻¹ and held isothermally for 40 min. The CH₄ flow was stopped after 20 min of isothermal treatment while maintaining the H₂ flow during the final 20 min followed by cooling down to room temperature. The samples were then passivated under 1% (v/v) O₂/He flow (50 mL min⁻¹) overnight before exposure to the atmosphere. The gas phase composition at the exit of the reactor was continuously monitored using a quadrupole mass spectrometer (Pfeifer GDS 320). The samples were coded as W_xC/C in the case of non-promoted tungsten carbide supported on carbon, 1Pd-W₂C/C and 2Pd-W₂C/C, promoted with 1 and 2wt.% of Pd, respectively.

XAS

X-ray absorption near-edge structure (XANES) and Extended X-Ray Absorption Fine Structure (EXAFS) at the Pd K-edge (24350 eV) were carried out at BM23 at the European Synchrotron Radiation Facility (ESRF). Data was collected in fluorescence mode using a 13 element Ge detector. The samples were placed in quartz capillaries of 1.5 mm diameter. The catalysts were carburized *in situ* under CH₄ (2 mL min⁻¹) and H₂ (18 mL min⁻¹) up to 850°C (10°C min⁻¹) and maintained at this temperature for 15 min. CH₄ was then removed from the atmosphere and the catalysts were kept at 850°C for an additional 10 min. The sample was then cooled down under hydrogen and three consecutive EXAFS spectra were collected and averaged for data analysis.

The EXAFS oscillations of two samples were analyzed: 1Pd-W₂C/C and 2Pd-W₂C/C. EXAFS oscillations were extracted using Athena code and analyzed using Artemis software³¹. The range used to transform the EXAFS oscillations ($k^2 \chi(k)$) was $\Delta k = (3-8.5) \text{ \AA}^{-1}$ and the fits were performed in the interval $\Delta R = (1.5-3.2) \text{ \AA}$.

The local environment of the Pd atoms was determined using the phase shift and amplitude functions for Pd-Pd calculated for Pd⁰. An additional Pd-W contribution was included to improve the fit. The calculation was done via randomly substituting 6 Pd atoms in the first coordination shell of the Pd⁰ structure by W. A test was also performed including Pd-C, Pd-O or Pd-Cl with the Pd-Pd contribution.

The photoelectron energy origin correction (ΔE_0) and the passive electron amplitude reduction factor (S_0^2) were found for Pd⁰ standard and used as fixed parameters to fit the samples. For each contribution, a coordination number (N_i) and a distance (R_i) were fitted independently while the mean square relative displacement (σ_i^2) were set to be the same for all paths.

In-situ XRD

The *in-situ* XRD analysis measured during the carburization process was performed at the I11-High Resolution PXRD beamline at Diamond Light Source (UK) using a sapphire capillary cell, hot air blower and PSD detectors. The carburization was carried out under a total flow of 20 mL min⁻¹ of 10% CH₄/H₂ gas mixture. The samples were heated to 999°C using a heating rate of 8°C min⁻¹ in order to determine the carburization

temperature of each sample. The experiments were performed at 15 KeV with 2θ ranging from 3-150°.

Ex-situ XRD analyses were obtained at the XPD beamline at the Brazilian Synchrotron Light Laboratory (LNLS). A wavelength of 1.62551 Å was used and the XRD patterns were obtained via a Mythen - 1K detector (Dectris) installed 1 m from the sample. Identification of crystalline phases was obtained by comparison to the JCPDS files. The full width at half maximum (FWHM) of the peaks was determined using a pseudo-Voigt function with the crystal size for tungsten carbide phases estimated using the Scherrer equation.

XPS

X-ray Photoelectric Spectroscopy (XPS) measurements were performed at the LNLS using an electron analyzer SPECS, model Phoibos HSA-3500 150, with Al K α radiation (1486.61 eV), pass energy of 20 eV and 14 h acquisition. The powdered samples were supported on copper double-sided tape and fixed on the XPS sample holder. The spectra were analyzed using Casa XPS software, version 2.2.99. The binding energies were referenced to the C 1s line at 284.5 eV from carbon. The curve-fittings used in the deconvolution for W 4f, Pd 3d, O 1s and C 1s levels were Gaussian line shapes using the Shirley function in the background simulation. The quantitative evaluation of each peak was calculated by dividing the integrated areas under the peak by the atomic sensitivity factors considering 1.0 the sensitivity factor of C 1s (binding energy of the 284.5 eV).

HR-TEM and SI-XEDS

The morphology of the Pd-W₂C/C crystallites was investigated by HR-TEM using a JEM 2100F microscope (JEOL) operated at 200 kV at the LNNano/CNPEM, with a point-to point resolution of 0.19 nm. Samples were prepared by applying the dry Pd-W₂C/C powder onto a carbon film surface of standard 400 mesh TEM cooper grids. Catalyst compositional maps were acquired by XEDS-SI with an AZtec 3.0 SP2 (Oxford Instruments) system. Electron probe size of ca. 0.7 nm was used to guarantee enough current density at each sample point, in order to obtain statistically significant X-ray counts for the elements of interest. SIs were acquired by scanning an area of interest of the sample with a pixel size of ca. 0.5 nm and a total dwell time of 0.6 s/pixel. Complete XED-spectra were acquired at each SI pixel in the 0-20 keV energy range.

N₂ Physisorption

Surface area and pore volume were determined by adsorption-desorption isotherms of N₂ at 77 K (-196 °C) using a Quantachrome Autosorb 1C automatic analyzer. The wet samples were degassed at 120 °C for 12 h before the isotherms were measured. The apparent BET surface area was determined by BET method using a multipoint method from the data collected at the relative pressures $0.1 \leq P/P_0 \leq 0.25$ due to the presence of micropores in the samples. The total pore volume was derived from the amount of gas adsorbed at a relative pressure of $P/P_0 = 0.95$. The pore size distribution was determined using BJH method.^{32,33}

Cellulose Conversion Reactions

The cellulose catalytic reactions were conducted using a stainless steel batch reactor (300 mL, Parr Instruments) at 4.3 MPa of H₂, 150 mL of an aqueous suspension contain 1 g (dry basis) of cellulose (Avicel microcrystalline Merck) and 0.300 g of catalyst. Details of the catalytic reaction are reported elsewhere²⁰. The reactions were performed at 190, 220 and 250 °C and the reaction time varied from 0 to 180 min.

HPLC analysis were performed using a Waters 1525 chromatograph at the CTBE/CNPEM equipped with Aminex HPX-87H – Bio-rad capillary column and Acclaim 120 C18 Dionex column for analysis using refractive index (RI) and UV detectors.

A quantitative method using thermogravimetric analysis (TGA) has been developed to determine the quantity of cellulose after a catalytic reaction, which was used to calculate cellulose conversion³⁴.

Cellulose conversion (X) and product yield (PY) were determined according to the equations:

$$X (\%) = \left(\frac{CM_{(i)} - CM_{(f)}}{CM_{(i)}} \right) \times 100\%$$

$$PY (\% \text{ mol C}) = \left(\frac{n_j C_j}{n_{cel} C_{(i)}} \right) \times 100\%$$

where $CM_{(i)}$ is the dry cellulose mass measured prior to the catalytic reaction, $CM_{(f)}$ is the dry cellulose mass measured after catalytic reaction, $n_j C_j$ is the amount of moles of carbon

of identified product j (acetol, ethylene glycol, 1,2-propylene glycol, etc.), $n_{\text{cel}}C_{(i)}$ is the amount of moles of carbon carried in the reactor .

3. Results and Discussion

3.1 Characterization

XAS

XAS measurements were performed to investigate the local structure and oxidation state of Pd in the catalyst after the carburization under hydrogen flow. The Fourier transform (FT) of the EXAFS spectra at the Pd k-edge of the 1Pd-W₂C/C and 2Pd-W₂C/C samples are shown in the supplementary material, Fig. S5. The EXAFS quantitative parameters derived from the fitting are presented in Table 1.

Both samples exhibited smaller coordination numbers (N) (Table 1) compared to Pd bulk (N=12), indicating the presence of nanosized Pd particles. This is also reinforced by the high value obtained for the Debye-Waller factor (σ^2), which is characteristic of high degree of disorder in the Pd lattice.

Interestingly, the EXAFS simulations for both samples improved when Pd-W contributions were added. This indicates that palladium nanoparticles are interacting with W in the catalyst. Moreover, an increase in the Pd-Pd interatomic distance ($R_{\text{Pd-Pd}}$) was observed compared to Pd⁰ (2.75 Å) (Table 1). This is in agreement with the presence of very small Pd particles, which are exposed to hydrogen³⁵. Palladium lattice expansion during thermal treatment under hydrogen has been reported³⁵⁻³⁹ and it likely in this case due to the final step of the carburization process at 850°C under H₂ flow.

Table 1. EXAFS fit results for the first coordination shell of the Pd in the Pd-promoted tungsten carbide catalysts after the carburization process under H₂ flow.

Sample	$N_{\text{Pd-Pd}}^*$	$N_{\text{Pd-W}}^*$	$R_{\text{Pd-Pd}}$ (Å)	$R_{\text{Pd-W}}$ (Å)	$\sigma^2_{\text{Pd-Pd/Pd-W}}$ (Å ²)
1Pd-W ₂ C/C	4 ± 2	3 ± 2	2.78 ± 0.01	2.91 ± 0.02	0.011 ± 0.005
2Pd-W ₂ C/C	4 ± 3	3 ± 3	2.77 ± 0.04	2.90 ± 0.08	

$E_0 = 4$, amp = 0.83.

*High values in the errors of the coordination numbers are due to the high correlation between N and σ^2 .

The intensity of the XANES spectra of the 1Pd-W₂C/C shows enhanced damping compared to the Pd⁰ foil in Figure 1 (b). This shows structural disorder and/or nanosize structures, as already determined by EXAFS analysis (Fig. S6 and Table 1). Furthermore, theoretical calculations of the palladium electronic structure indicate that the increase in intensity of feature B is associated with the mixing of Pd d-states with hydrogen s- and p-unoccupied states³⁷. This may be associated with Pd nanoparticles and H₂ interaction, as also pointed out by EXAFS analysis.

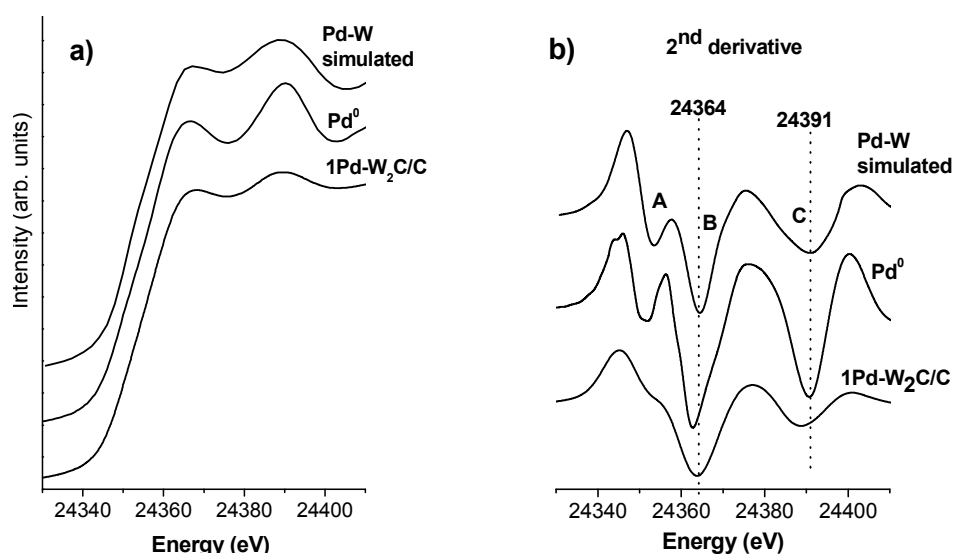


Figure 1. (a) Experimental XANES spectra of Pd⁰ and 1Pd-W₂C/C sample and simulated XANES spectra of Pd-W and (b) corresponding second derivatives.

Feature A, at lower energy is assigned as a d-peak, associated with 1s → 4d transitions, giving rise to pre-edge features in the XANES spectra⁴⁰. Features B and C are assigned to p-peaks, which correspond to s → p transitions⁴⁰. The main feature (B) corresponds to the absorption edge and reflects dipole-allowed Pd 1s → 5p transitions. Peak (C) is associated with shakeup processes involving Pd 1s → 5p transitions or multiple scattering⁴¹ and also 5p → 4f transitions³⁶.

Comparing the positions of feature B, the 1Pd-W₂C/C catalyst coincides with the simulated Pd-W specie, agreeing with the presence of Pd nanoparticles in contact with W in the sample. Additionally, an energy reduction in feature C could point to a slightly increased electron density in the external orbitals of the Pd³⁶, which is related to the interaction of Pd and hydrogen.

XRD

In-situ XRD analyses were conducted to investigate the influence of Pd on the carburization temperature, carbide phase formation and crystallinity of the samples.

In general, the carburization process follows the steps: $\text{WO}_3 \rightarrow \text{WO}_x$ ($3 > x > 2$) $\rightarrow \text{WO}_2 \rightarrow \text{W} \rightarrow \text{W}_2\text{C} \rightarrow \text{WC}$ ^{20,42-45}. The *in-situ* XRD results showed the formation of metallic W at $\approx 561^\circ\text{C}$ and the carbide W_2C phase transition occurring at $\approx 805^\circ\text{C}$ (Fig. 2). The W_2C phase can clearly be identified as well as the peaks related to Pd species.

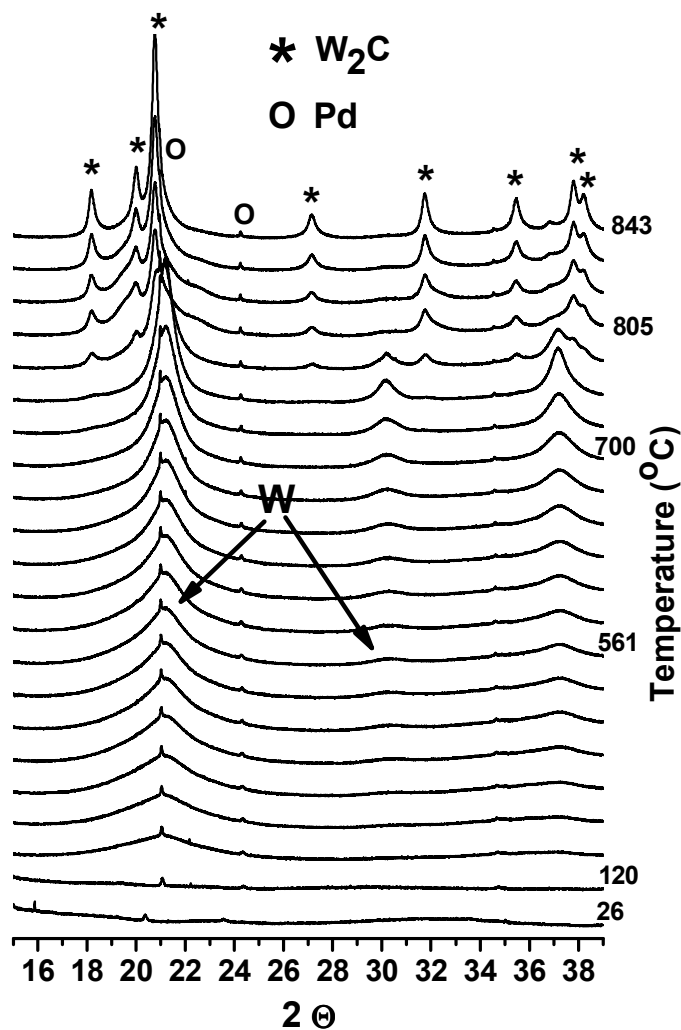


Figure 2. *In-situ* carburization of Pd promoted tungsten carbide catalyst supported on activated carbon (2Pd-W_xC/C). XRD patterns were collected at a wavelength, $\lambda = 0.82656\text{\AA}$.

In a previous work²⁰, *in-situ* XRD analysis of the non-promoted tungsten carbide catalyst showed that metallic tungsten was formed at higher temperature ($\approx 690^\circ\text{C}$) with

carbide formation happening at similar carburization temperature ($\approx 850^\circ\text{C}$). Moreover, a mixture of three nanosized carbide phases W_2C , WC_{1-x} , and WC were formed. However, when Ni was used as a promoter, the carburization temperature was reduced by 100°C and much like the Pd-promoted catalysts studied here, only the W_2C phase was formed.

XRD patterns of all samples after the carburization process at 850°C are shown in Fig. 3. The predominant carbide phase in the promoted catalysts is W_2C , while in absence of palladium, a mixture of carbide phases are formed. Nano-crystalline palladium is also formed during the carburization, corroborating with XAS results.

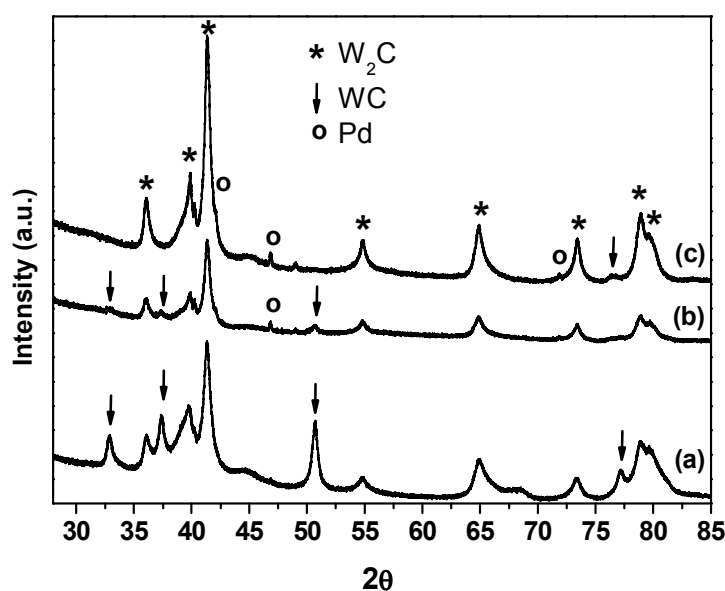


Figure 3. XRD analysis of (a) $\text{W}_x\text{C}/\text{C}$; (b) $1\text{Pd}-\text{W}_2\text{C}/\text{C}$; (c) $2\text{Pd}-\text{W}_2\text{C}/\text{C}$. XRD patterns were collected at $\lambda=1.6255\text{\AA}$.

XPS

The W 4f core-shell spectra of the catalysts are shown in Fig. S6. XPS analysis shows only tungsten oxide species on the surface of the Pd-promoted catalysts after the carburization and passivation. Only the non-promoted sample exhibits very small doublet peaks related to tungsten carbide species, which may indicate a thinner oxide layer on the surface of the catalyst²⁰.

The XPS spectra in Fig. S7 shows the Pd 3d core-level spectra characterized by two components, Pd $3d_{5/2}$ and Pd $3d_{3/2}$, which appear due to spin-orbital splitting. The noise and

weak signal can be related to the low Pd loading (1 and 2wt.%) and/or carbon deposition. The binding energies of the Pd 3d_{3/2} peaks around 336 and 336.7 eV, respectively, are related to palladium oxide species⁴⁶, which is in accordance with the carburization and passivation process applied in the catalysts synthesis.

Table 2: Relative surface concentration between W and C determined by XPS analysis ($\pm 2\%$ error).

Catalyst	W/C ratio
W _x C/C	0.028
1Pd-W _x C/C	0.035
2Pd-W _x C/C	0.038

The relative surface concentration was determined considering only the presence of W and C on the surface. The Pd loadings are lower than the detection limit of the XPS. According to quantitative XPS analysis (Table 2), a significant increase in the concentration of W on the surface is observed in both of the Pd-promoted tungsten carbides, which indicates that more tungsten was exposed on the surface in the promoted-catalysts in comparison with the non-promoted.

HR-TEM and SI-XEDS analysis

Bright-field (BF) TEM images of the 2Pd-W₂C/C catalyst revealed a bimodal distribution of particle sizes. BF-STEM images (Fig. 4A, C and D) show extensive regions with a large number of small particles (< 10 nm), homogeneously distributed over the support, along with a second population of larger particles varying in size from 20 to 100 nm (Fig. 4A, B, and D). These large particles have a core-shell structure, with a dark core and a gray shell. The contrast of the HAADF image (Fig. 4E) is taken from the same area as Fig. 4D and has been inverted, revealing a particle structure with a high Z atomic number core surrounded by a lower Z shell. XEDS chemical mapping (Fig. 4F and S10) and HR-TEM images (Fig. S9) of the larger particles show a crystalline core enriched with W, which is surrounded by a shell formed by small crystallites giving a mixture of W and Pd. Interestingly, Pd was dispersed widely over the sample as well as W. Importantly, filamentous and/or graphitic carbon was not detected on the catalyst surface (Fig. S9).

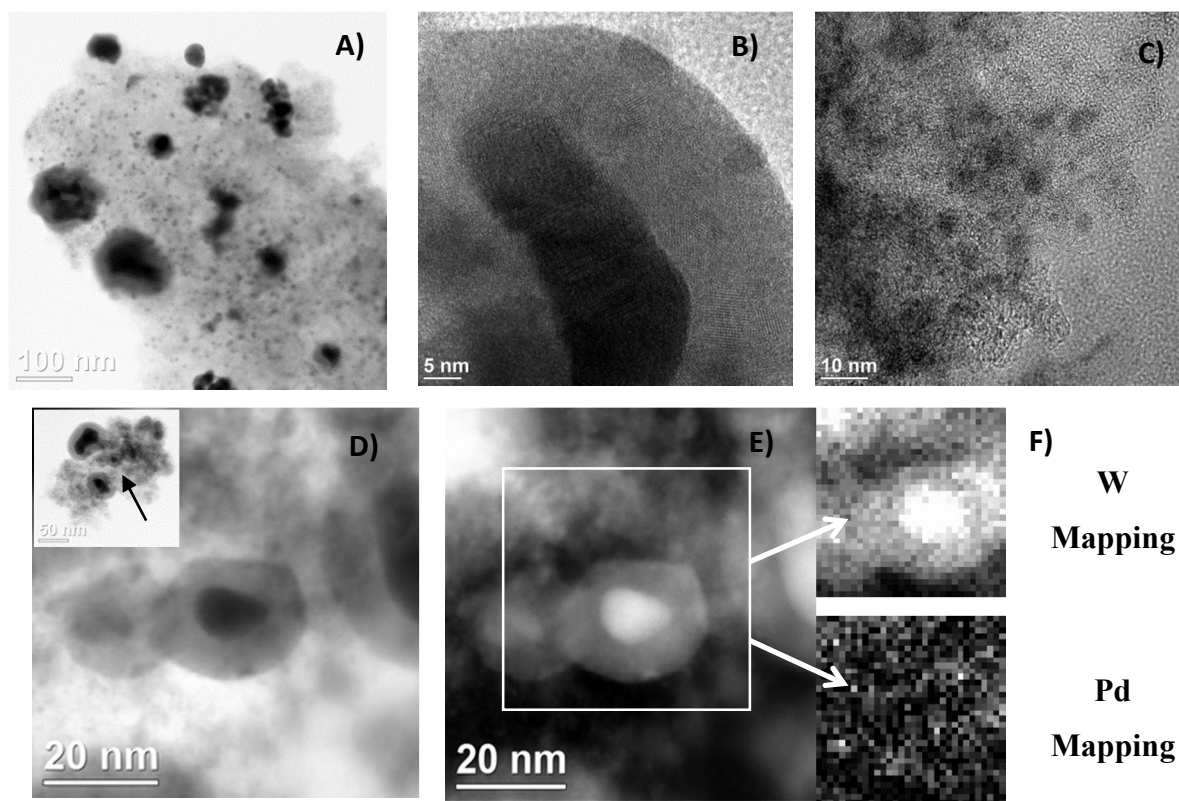


Figure 4. Bright-field STEM (A and D), BF-HR-TEM (B and C), HAADF-STEM (E) images and SI-XEDS chemical mapping (F) of the Pd-promoted tungsten carbide catalyst. Insert of figure (D) shows a low magnification BF image of a carbon grain, with the arrow indicating the central particle shown in higher magnification in (D).

N₂ Physisorption

Apparent BET surface area and pore volume values decreased with increasing Pd loading in the samples (Table 3). The mean pore diameter was the same for all samples. The adsorption-desorption isotherms are characteristic of materials comprising both micro and mesoporosity (Fig. S1) as expected for an activated carbon (70wt% of the catalyst). However, the adsorption volume at low relative pressure ($P/P_0 \leq 0.1$), the pore size distribution (SI Fig. S2) as well as total adsorption capacity ($P/P_0 \approx 1$) decrease when Pd loading increases. This shows that the activated carbon and consequently the catalyst microporosity and surface were affected by the carburization process of the tungsten.

Table 3: N₂ physisorption analysis.

Catalyst	Apparent BET Surface Area (m ² g ⁻¹)	Total pore volume (cm ³ g ⁻¹)	Mean pore diameter (Å)
W _x C/C	649	0.577	38
1Pd-W ₂ C/C	502	0.490	39
2Pd-W ₂ C/C	366	0.340	38

There are two fundamental steps in the carburization process: i) tungsten oxide reduction and ii) tungsten carburization^{13,16,20,42,43}. Due to the hydrogen spillover ability exhibited by metals, such as Ni, Co, Pt and Pd the reduction of tungsten occurs at lower temperature when compared with non-promoted catalysts^{13,16,18,20,42,43}. The same trend was observed here, the *in-situ* XRD analysis revealed that crystallites of metallic tungsten were formed around 561 °C in the 2Pd-W_xC/C as well as our previous work with Ni-promoted catalysts²⁰. In the non-promoted catalyst case tungsten was only formed above 690 °C²⁰. Furthermore, besides the reduction step, the activated hydrogen should play a role in the second step of the carburization where it may interact with the carbon from the support and/or the CH₄ to form CH_x and C* species. These species are also formed through the thermodynamic decomposition of methane. According to Giraudon et al.⁴⁷, the species are adsorbed onto the W surface and carbon is inserted into the W lattice to produce the carbide phases.

Another factor to consider is the promoter interaction with CH₄ and its effect on the carburization. Density functional theory (DFT) studies by Kai Li et al.²⁶, showed that CH_x (1 ≤ x ≤ 4) decomposition is an endothermic process. Therefore, the reaction energy as well as the energy barrier is lower with Ni than that of Pd. Thus, the methane decomposition is thermodynamically and kinetically favoured in a Ni promoted catalyst. This explains the higher carburization temperature in the Pd-promoted tungsten carbide catalysts when compared to the Ni-promoted catalysts previously studied²⁰. The mass spectrometry results obtained during the carburization process (Fig. S4-S5) also show an increase in CH₄ production at 850 °C for the Pd-promoted and the non-promoted catalyst. The methane level at 850 °C is higher than its inlet flow at lower temperatures up to 400 °C. This implies that atomic carbon from the catalyst support (C*) may be interacting with H₂ to form CH₄

in the gas phase, which flows off the catalyst bed and consequently, from the catalyst surface. This result is confirmed by TEM (Fig. 4) and XPS results (Table 2), showing that the Pd and tungsten carbide particles are not covered by carbon with W being more exposed on the surface in the Pd-promoted catalysts. The results indicate that the main carbon source in the carburization process of the Pd-promoted catalysts is the activated carbon itself. According to the N₂ physisorption analysis, the microporosity was affected by the carbothermal process^{13,20,43}, giving lower surface area, total pore volume and lower adsorption capacity (Table 3). On the other hand, an intense CH_x decomposition and carbon deposition was identified in our previous work with Ni-promoted tungsten carbide^{20,29,48}, resulting in a lower carburization temperature and less sintered W₂C particles (Fig. S9). However, Ni is also highly active in forming polymeric, filamentous and graphitic carbon deposits on the catalyst surface, which inhibits the active sites of the catalysts^{13,16,18,20,42–45}.

3. 2 Catalytic Performance

Catalytic activity of 1 and 2 wt.% Pd-promoted tungsten carbide catalysts were evaluated at 190, 220 and 250°C as a function of reaction time. Conversion and product distribution results are shown in Figures 5, 6 and 7.

The identified reaction products consisted of ethylene glycol (EG), 1,2-propylene glycol (1,2-PG) and acetol for all reaction temperatures. In addition, glucose, sorbitol, methanol, ethanol, 1-propanol, 1-butanol and levulinic acid were also analyzed. Glucose was not detected in any of the experiments performed, which indicates the catalyst high reactivity under the catalytic parameters tested.

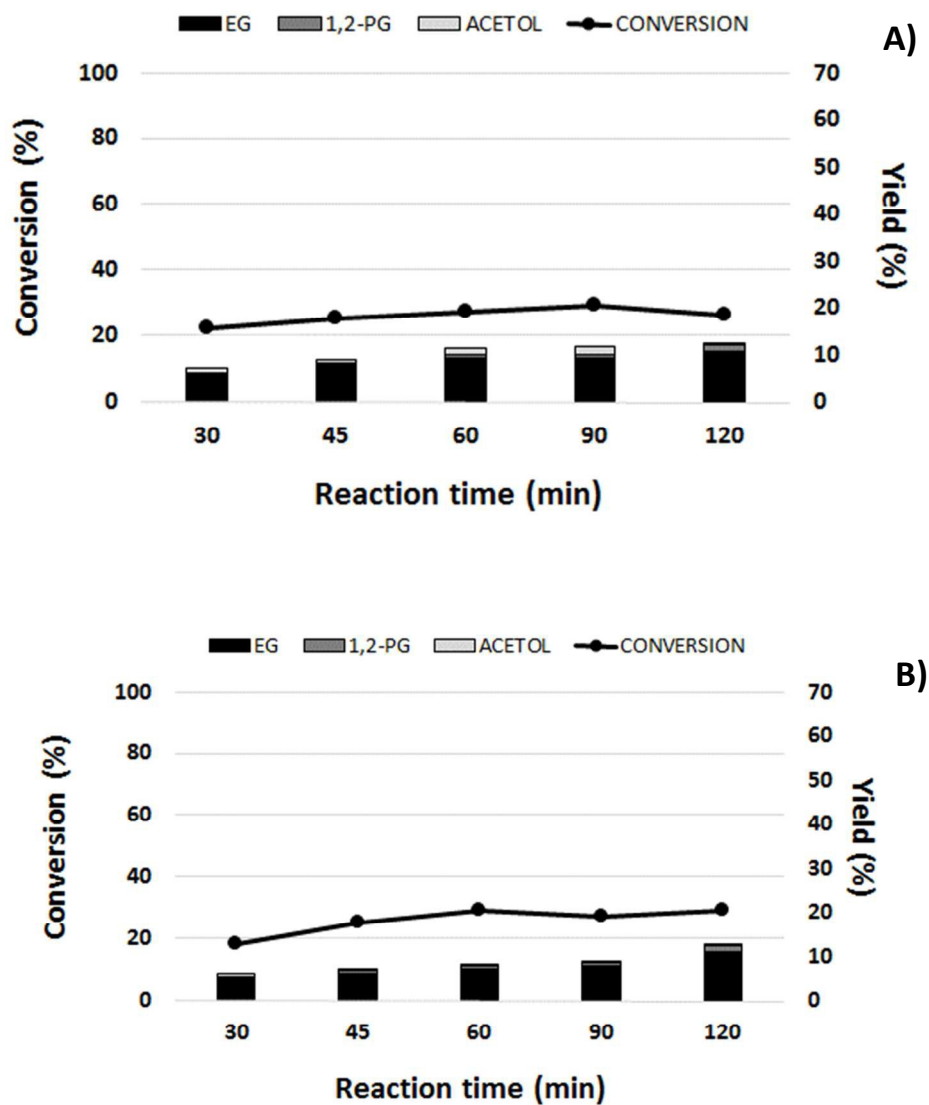


Figure 5: Catalytic activity for the conversion of cellulose and yields of EG, 1,2-PG and acetol for reactions at 190°C for A) 1Pd-W₂C/C and B) 2Pd-W₂C/C.

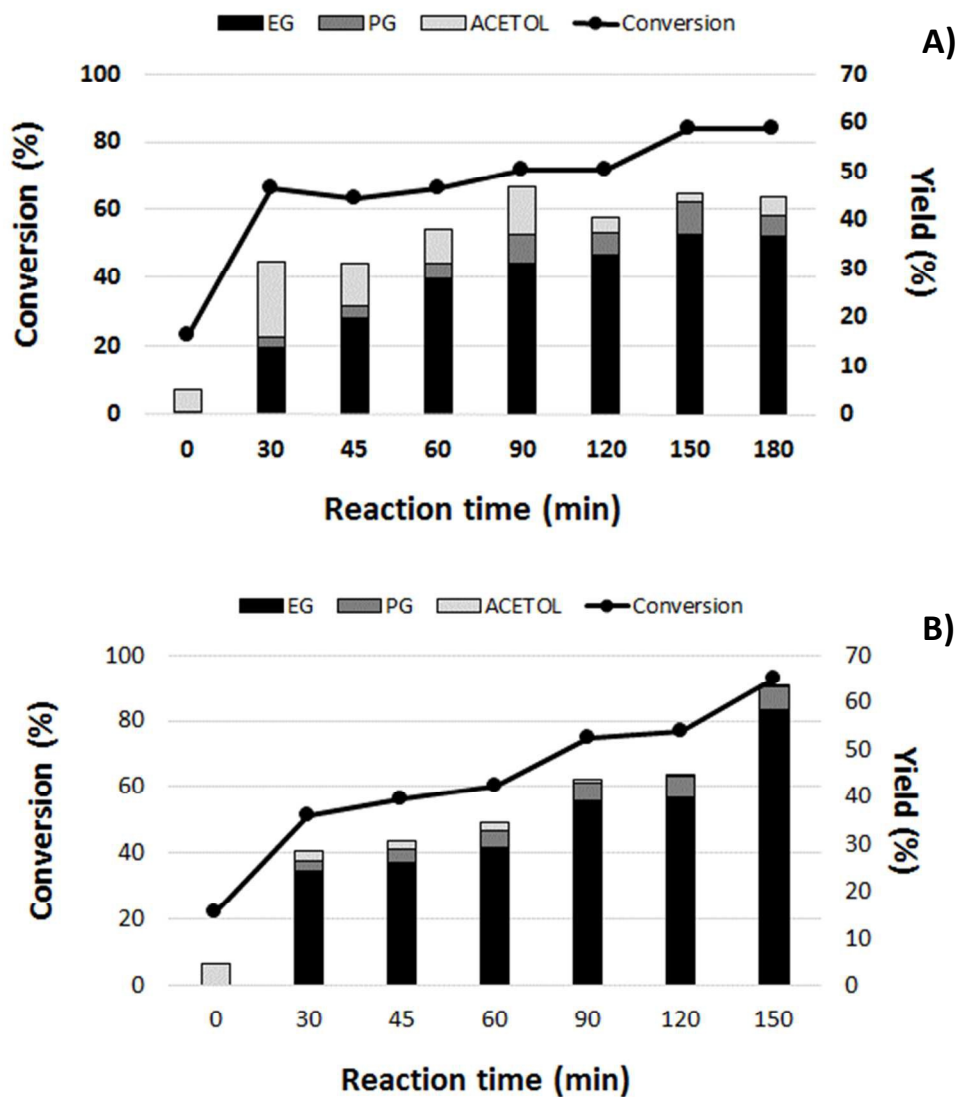


Figure 6: Catalytic activity for the conversion of cellulose and yields of EG, 1,2-PG and acetol for reactions at 220°C for A) 1Pd-W₂C/C and B) 2Pd-W₂C/C.

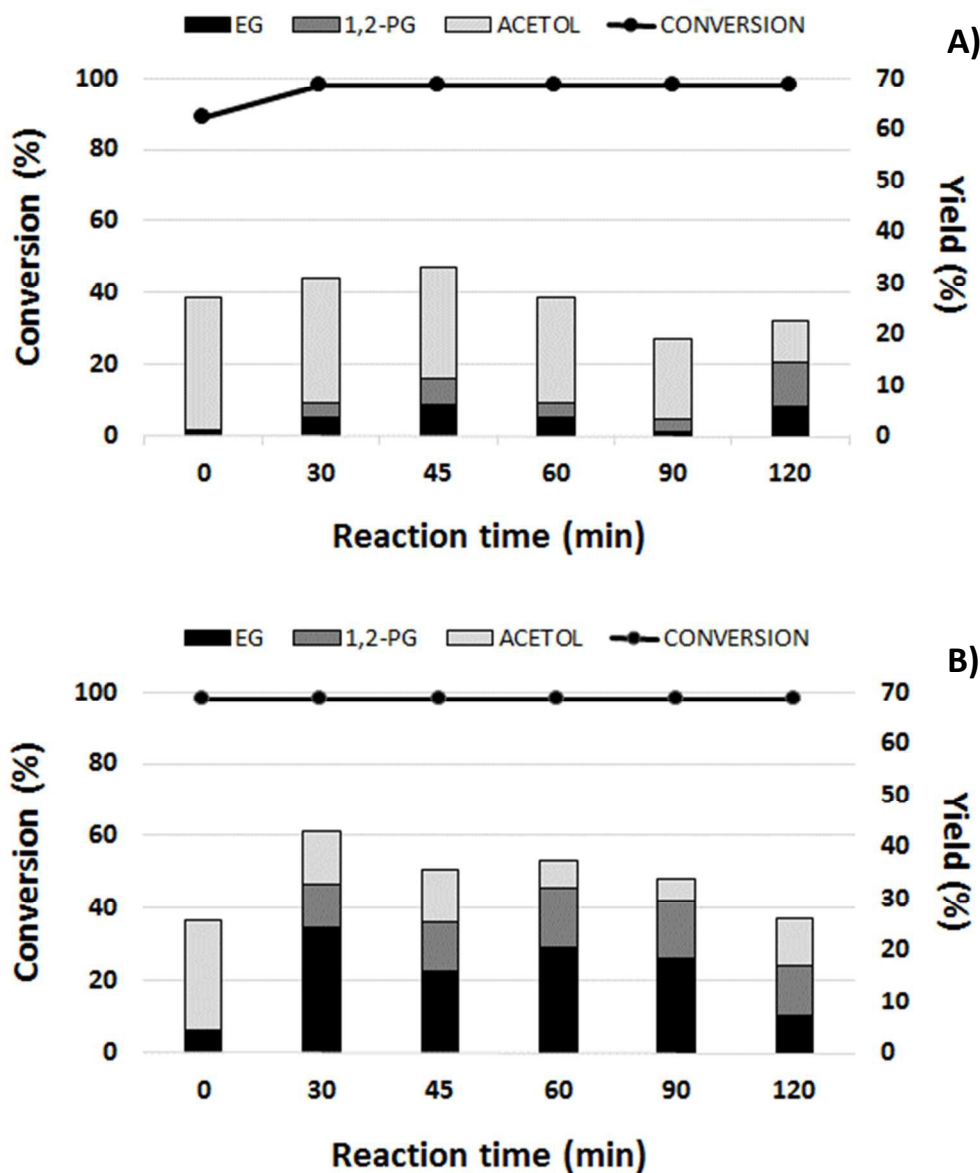


Figure 7: Catalytic activity for the conversion of cellulose and yields of EG, 1,2-PG and acetol for reactions at 250 °C for A) 1Pd-W₂C/C and B) 2Pd-W₂C/C.

In general, conversion increased as reaction temperature increased. Taking into account the longer reaction time, conversion improved from ~30% to ~94% when the reaction temperature increased from 190°C to 220°C and reached 100% at 250°C. Cellulose reactions carried out at 190 °C (Fig. 5) showed similar performances for both catalysts, giving low conversion values with a slight increase after 120 min. EG was the

major product, with a maximum yield of ~10% for both catalysts. 1,2-PG, acetol, sorbitol, ethanol and levulinic acid were also detected with yields lower than 1.5%.

These results are in agreement with previous studies of catalysts based on tungsten carbide in a one-pot cellulose reaction at low temperature as 190°C^{13,49}. It is notable that in the case of noble metals or bimetallic catalysts applied in cellulose hydrogenation reactions, sugar alcohols, like hexitols, are the preferred product formed^{23,24}

Notably, results from the catalytic reaction carried out at 220°C showed the conversion increasing considerably with reaction time, especially when the 2% Pd-W₂C/C catalyst is considered. Cellulose conversion reached 94% for 2% Pd-W₂C/C in 150 min and 84% for the 1% Pd-W₂C/C catalyst after 180 min of reaction.

Interestingly, both catalysts gave 20% conversion at time zero of the reaction. Time zero corresponds to the reactor heating period under a low hydrogen pressure of 50 psi. Once the reaction temperature was reached (220°C), the hydrogen pressure was immediately increased to 800 psi and the reaction time taken as zero at this point. For both samples, during this initial heating step, acetol was obtained as the major product (~4.5% yield) and EG production was negligible.

The conversion increased ~2.5 times after 30 min of reaction. The product distribution changed due to hydrogen availability, as expected, but also because of the Pd content in the catalyst (Fig. 6 A and B). When the 1Pd-W₂C/C sample was used, EG yield increased, especially during the 60 min of reaction (~28%), reaching its highest value ~37% after 150 min (84% of conversion). Acetol yield followed the opposite trend, forming the major product with a yield of ~15% in the first 30 min but decreased to ~4% after 150 min. Over the same reaction time interval 1,2-PG increased from ~2 to 7%. It is well known that acetol is an intermediate in 1,2-PG formation from sugars and cellulose¹⁵. Thus, acetol was hydrogenated to 1,2-PG, in agreement with literature^{17,30,50}.

In the case of the 2wt.% Pd-promoted catalyst, EG production was more favored. EG increased from ~24 (30 min) to ~58% in 150 min of reaction while the conversion varied from 51 to 93%. Moreover, acetol depletion was followed by the 1,2-PG formation with more pronounced formation after 90 min of reaction.

Ethanol (~6%) and levulinic acid (~4%) was observed as secondary products with similar yields for both catalysts. Methanol, 1-propanol and 1-butanol were also detected in

trace quantities. The presence of shorter chain alcohols, organic acids and other products such as furans and CO₂ can be attributed to subsequent degradation reactions of monosaccharides as well as reaction intermediates, which can undergo further hydrolysis and hydrogenolysis of C–O and C–C bonds under the reaction conditions^{13,19,51,52}.

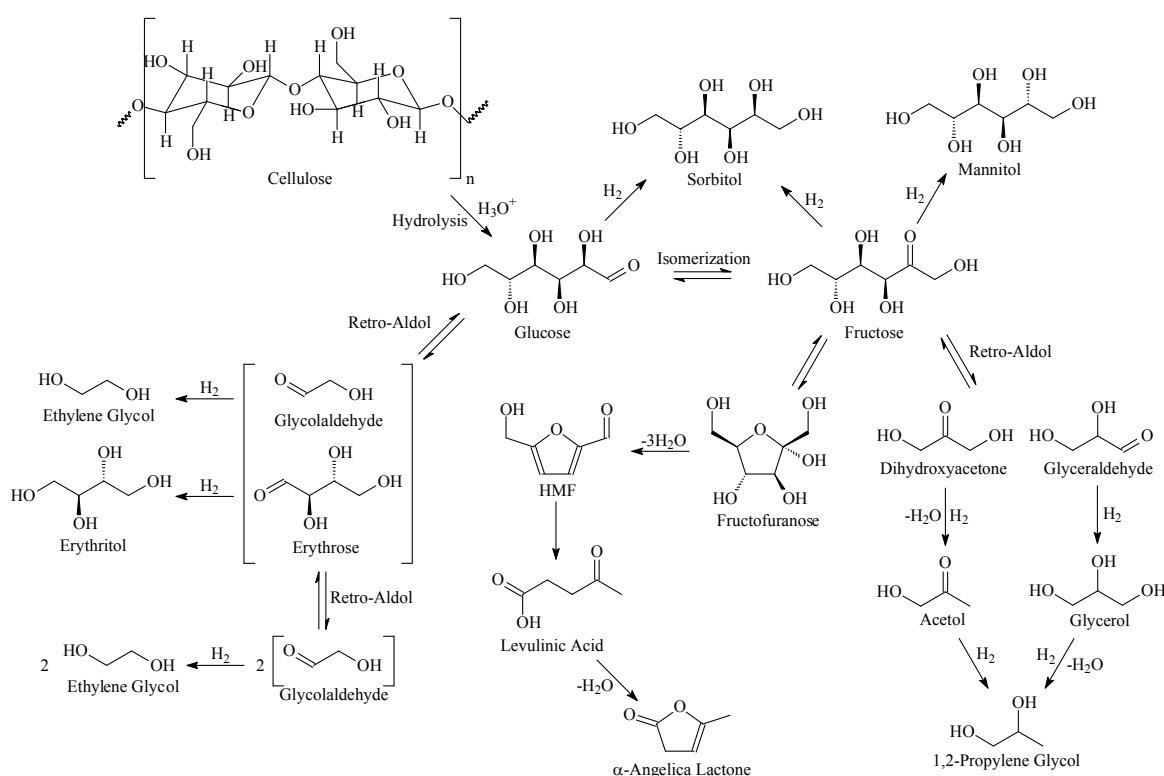
Reactions performed at 250°C with both catalysts gave 100% cellulose conversion after 30 min of reaction. Acetol was the main detected product during the reactor heating step (at time 0). Since H₂ partial pressure is low (50 psi) the catalyst containing 2wt.% of Pd exhibited higher EG yields compared to 1wt.% of the Pd-promoted catalyst. This tendency was emphasized once the H₂ pressure was increase and at longer reaction times. It indicates a higher hydrogenation efficiency of the catalyst when 2% of Pd was used in the tungsten carbide catalyst. On the other hand, acetol hydrogenation to 1,2 PG and other degradation products also took place at 250°C for both catalysts but was more pronounced in the case of the 1Pd-W₂C/C catalyst. It was also observed that an increase in the quantity of secondary products when compared at milder temperatures. Yields of levulinic acid, 1-butanol, 1-propanol, ethanol and methanol were approximately 8%, 2%, 4%, 3% and 1% respectively, with similar results for both catalysts.

The catalytic conversion of cellulose in a one-pot reaction involves various reaction pathways as showed in Scheme 1. Firstly, cellulose is hydrolyzed to form oligomers and glucose. This step is controlled by the H⁺ ions generated from the hot water and also from the acidic surface properties of the catalyst^{10,20}. Secondly, glucose can be transformed into a variety of intermediates and products by various side reactions. These routes are strictly dependent on the catalytic properties of the catalyst as well as the reaction parameters^{15,17,19–21,50,53,54}.

Supported metallic catalysts such as Ru/C and Pt/C readily transform glucose into sugar alcohols by the reduction of the carbonyl groups on the glucose with H₂ on the metallic active site leading to the formation of hydrogenated products such as sorbitol and mannitol^{10,23,24,55}. Here, sorbitol was detected in a concentration lower than 1.5%, indicating that the direct glucose hydrogenation was not favored under the reaction conditions.

Metal promoted tungsten carbides are considered multifunctional catalysts providing high EG yields from cellulose in one-pot reactions. The catalyst is selective in

transforming glucose into glycolaldehyde through a retro-aldol reaction catalyzed by tungsten carbide. Secondly, the glycolaldehyde can be hydrogenated to EG over the metallic promoter and W_2C active sites of the catalyst^{13,15,20,21,24,53}. Glucose can be also isomerized to fructose in the reaction conditions. Furthermore, acetol can be obtained by fructose transformation through a retro-aldol reaction on the tungsten carbide sites¹⁵. This was observed at time zero of the reaction at 220 and 250°C (Fig. 6 and 7), exhibiting acetol as the major product. Once hydrogen pressure is added in the catalytic reaction, acetol and glycolaldehyde (not identified) are hydrogenated to 1,2-PG and EG, respectively by Pd and W active sites.



Scheme 1: Reactions pathways in cellulose conversion, adapted from^{15,19}.

The stability of the major products, EG and acetol, were tested under the catalytic conditions given in table 4. EG degraded somewhat over time but was much more stable than acetol. Acetol underwent hydrogenation to 1,2-PG in high proportions. Our results are in agreement with previous studies with tungsten based catalysts^{15,21,50}.

Table 4: Catalytic activity of Pd-W₂C/C over different substrates. Reactions conditions: 220°C, 150 min, 4 MPa of H₂.

Substrate	Conversion (%)	Product Yield (% mol C)					MB*
		EG	1,2-PG	Acetol	Ethanol	Lev. Ac.	
Cellulose	84	36.9	6.6	1.7	6.1	6.0	60.3
Acetol	71	-	55.4	-	1.7	-	58.4
EG	6	-	-	-	-	-	-

*MB = Mass Balance. Low quantities of methanol, 1-propanol and butanol were detected which are not reported in the table.

The contribution of tungsten and palladium species on the conversion of cellulose over activated carbon, non-promoted tungsten carbide catalyst (W_xC/C) and 1% wt. Pd supported on activated carbon (1Pd/C) was also performed. The activated carbon, used as the catalytic support, was also tested in order to determine its contribution to cellulose conversion. The results are shown in Table 5.

Table 5: Cellulose conversion and product yields over different catalysts. Reaction conditions: 220°C, 150 min, 4 MPa H₂.

Entry	Catalyst	Conversion (%)	Product Yield (% mol C)					MB*
			EG	1,2-PG	Acetol	Ethanol	Lev. Ac.	
1	W _x C/C	89	1.7	0.3	22.5	1.1	0.6	28.6
2	1% Pd/C	73	1.7	0.1	20.5	0.0	1.2	24.7
3	1Pd-W ₂ C/C	86	36.9	6.6	1.7	6.1	6.0	60.3
4	2Pd-W ₂ C/C	93	58.2	4.9	0.4	0.1	3.6	67.5
5	C ^A	26	0	0	8.0	0	0.3	8.3

^A 60 min of reaction.

*MB = Mass Balance. Low quantities of methanol, 1-propanol and butanol were detected which are not reported in the table.

Despite providing relatively high and comparable cellulose conversion, both Pd/C and W_xC/C catalysts showed poor selectivity to EG (Table 5, entries 1 and 2). The combination of both metals to obtain a Pd-promoted tungsten carbide catalyst (1Pd-W₂C/C and 2Pd-W₂C/C) were able to achieve a high EG yield as shown in Table 5 (entry 3 and 4).

However, both tested catalysts performed retro-aldol reactions to produce acetol from cellulose (Entry 1 and 2). This was not expected from the 1% Pd/C catalyst due to its hydrogenation ability to convert glucose into sugar alcohols^{10,23,24,55}. However, the lower Pd concentration as well as the lower hydrogen pressure used seems to disfavor hydrogenation reactions. The activated carbon used as the support in all samples, when applied in a pure form in the cellulose conversion, gave low conversions (26%) and produced only a small quantity of acetol (8% yield).

Catalyst reusability is a key factor for industrial applications and due to the variety of recovery procedures and additional structural and catalytic investigations it should be considered as a separate study. Here, the evaluation of the potential reusability of the 2Pd-W₂C/C catalyst was performed. According to the XRD data obtained after the catalytic reaction (SI, Fig. S12), the majority of the W₂C phase as well as small and broad peaks relating to Pd⁰ remain, which indicates structural stability for long-term usage of the catalyst. However, the catalytic results in general exhibited lower conversion and selectivity to EG after 4 recycling runs (Fig. SI 11). The total polyol yield (EG + acetol + 1,2-PG) also decreased after 4 cycles. Due to the greasy nature of the catalyst after the catalytic reaction, even after multiple water washing procedures, evidence points towards non-reactive oligosaccharides or partially decomposed sugar and/or furans oligomers attached to the catalyst⁵⁶. These by-products were not removed during a simple water washing and probably blocked the catalysts active sites decreasing its efficiency. This result indicates that the washing process needs to be improved to remove by-products and recover the catalytic activity of the Pd-promoted tungsten carbide catalyst.

From the results presented here, it is clear that the tungsten carbide catalysts promoted with 2wt.% of Pd give the best catalytic performance under the reaction conditions tested. This system reached the highest EG yield (58%) at 220°C and 150 min of reaction. At higher temperature (250°C), competitive side reactions become more favored, which results in a less selective catalytic system towards EG production. However, the multifunctional catalyst still performs the retro-aldol reactions followed by hydrogenation. This catalytic property comes from the interaction between Pd and W₂C, which forms during the carburization process in the preparation steps of the catalyst. Using less promoter

(1wt.% Pd) in the catalytic system, the interaction between Pd and W_2C decreased, resulting in a multifunctional catalyst giving lower hydrogenation potential.

In terms of cellulose conversion and EG yield, Pd-promoted tungsten carbide catalysts are much more efficient than Ni-promoted catalysts when comparing the same cellulose conversion reaction parameters²⁰. 1Pd- W_2C/C and 2Pd- W_2C/C catalysts converted 72% and 75% of cellulose after 90 min of reaction time, producing ~31% and 39% EG yield, respectively, while 2% Ni-promoted tungsten carbide catalyst showed ~65% conversion and 26% EG yield. Moreover, Ni-promoted catalysts gave ~22% acetol yield, while 1% Pd and 2% Pd-promoted only gave 9.7 and 0.6,% respectively. These results point out a superior hydrogenation ability exhibited by Pd and W_2C interaction in the cellulose conversion reactions.

Characterization using *in-situ* XRD, XANES/EXAFS and EDS analysis (Fig. 1, 2 and Table 1), showed Pd and W interactions, as well as the formation of tungsten carbide W_2C phases during the carburization process. Pd nanoparticles help reduce the tungsten oxide to W^0 due to hydrogen spillover. Moreover, palladium is less thermodynamically and kinetically active towards CH_x ($1 \leq x \leq 4$) decomposition²⁶⁻²⁹. This hinders carbon deposition on the catalyst surface during the carburization, according to the XPS analysis and TEM. The carburization temperature did not decrease, as unanimously^{10,13,16,18,20,30,50,54,57,58} observed in the literature when Ni is applied as a promoter. Nickel favors the formation CH_x decomposition species, which contribute to increasing and speeding up the process of atomic carbon (C^*) formation and/or CH_x deposition on W surfaces for carburization. However, the catalytic as well as XPS results obtained here and in our previous work²⁰ show that a reduction in methane decomposition produces a cleaner catalyst surface and consequently, a higher conversion of cellulose. This gives Pd an advantage over Ni when its promotional effect on tungsten carbide is considered.

The catalytic efficiency as well as structural, surface and electronic properties of the Pd-promoted tungsten carbide catalysts have not been explored in the literature up to now. Only few catalytic tests are reported^{17,30}. From the studies here as well as in the well-explored Ni-promoted tungsten based catalyst studies^{10,13-20,30,49,50,54,57-60}, the interaction of the promoter and W_2C is a key point in the efficiency of cellulose conversion of towards EG production. Palladium hindered carbon deposition on the catalyst surface. Carbon

deposition is a drawback when transition metals carbide catalysts are considered^{20,42,43,45}. This may reveal a better and more profitable balance amongst catalyst cost, physical, chemical and catalytic properties to obtain higher EG selectivity from cellulose than Ni-promoted tungsten based catalysts.

Conclusions

The promotional effect of Pd on the tungsten carbide catalyst provided advantageous physical and chemical properties for catalytic application. A carbide catalyst with a cleaner and less inhibited surface was obtained due to less thermodynamically and kinetically active palladium reducing CH_x ($1 \leq x \leq 4$) decomposition during the carburization process. Thus, higher cellulose conversion was observed when compared to Ni-promoted tungsten carbide catalysts.

The interaction of Pd and W also enhances the ability of the catalyst to perform multi-step reactions resulting in higher conversion and selectivity towards ethylene glycol production. Thus, Pd seems to offer a better balance amongst catalyst composition, structural and surface properties as well as catalytic activity to obtain high value-added platform chemicals from cellulose.

Acknowledgements

The authors are grateful to LNLS/CNPEM and CAPES-CNPEM CNPq for the financial support, CTBE/CNPEM for chromatographic analysis of reaction products, LNNano for the TEM microscope and LNLS-Brazil and Diamond-UK for the synchrotron radiation facilities.

References

- 1 L. Hu, G. Zhao, W. Hao, X. Tang, Y. Sun, L. Lin and S. Liu, *RSC Adv.*, 2012, **2**, 11184.
- 2 M. J. Climent, A. Corma and S. Iborra, *Chem. Rev.*, 2011, **111**, 1072–133.
- 3 H. Cai, C. Li, A. Wang, T. Zhang, *Catal. Today* 2014, 234, 59-65.
- 4 J. J. Bozell and G. R. Petersen, *Green Chem.*, 2010, **12**, 539.
- 5 P. Gallezot, *Chem. Soc. Rev.*, 2012, **41**, 1538–58.
- 6 H. Kobayashi, T. Komanoya, S. K. Guha, K. Hara and A. Fukuoka, *Appl. Catal. A Gen.*, 2011, **409-410**, 13–20.
- 7 J. Ross, *Heterogeneous catalysis: fundamentals and applications*, Elsevier B.V.,

- 2012.
- 8 R. Rinaldi and F. Schüth, *Energy Environ. Sci.*, 2009, **2**, 610.
- 9 D. Alonso, J. Bond and J. Dumesic, *Green Chem.*, 2010.
- 10 M. Yabushita, H. Kobayashi and A. Fukuoka, *Appl. Catal. B Environ.*, 2014, **145**, 1–9.
- 11 M. L. and P. C. Katarína Fabičovicová, *Green Chem.*, 2015.
- 12 L. Negahdar, J. U. Oltmanns, S. Palkovits and R. Palkovits, *Appl. Catal. B Environ.*, 2014, **147**, 677–683.
- 13 N. Ji, T. Zhang, M. Zheng, A. Wang, H. Wang, X. Wang and J. G. Chen, *Angew. Chemie Int. Ed.*, 2008, **47**, 8510–8513.
- 14 G. Zhao, M. Zheng, A. Wang and T. Zhang, *Chin. J. Catal.*, 2010, **31**, 928–932.
- 15 L. Zhou, A. Wang, C. Li, M. Zheng and T. Zhang, *ChemSusChem*, 2012, **5**, 932–938.
- 16 Y. Zhang, A. Wang and T. Zhang, *Chem. Commun.*, 2010, **46**, 862–864.
- 17 A. Wang and T. Zhang, *Acc. Chem. Res.*, 2013, **46**, 1377–1386.
- 18 N. Ji, M. Zheng, A. Wang, T. Zhang and J. G. Chen, *ChemSusChem*, 2012, **5**, 939–944.
- 19 R. Ooms, M. Dusselier, J. a. Geboers, B. Op de Beek, R. Verhaeven, E. Gobechiya, J. a Martens, A. Redl and B. F. Sels, *Green Chem.*, 2014, **16**, 695–707.
- 20 C. B. Rodella, D. H. Barrett, S. F. Moya, S. J. a. Figueroa, M. T. B. Pimenta, A. A. S. Curvelo and V. Teixeira da Silva, *RSC Adv.*, 2015, **5**, 23874–23885.
- 21 J. Wang, G. Yao, Y. Wang, H. Zhang, Z. Huo and F. Jin, *RSC Adv.*, 2015, **5**, 51435–51439.
- 22 A. L. Dantas Ramos, P. D. S. Alves, D. a. G. Aranda and M. Schmal, *Appl. Catal. A Gen.*, 2004, **277**, 71–81.
- 23 H. Kobayashi, T. Komanoya, S. K. Guha, K. Hara and A. Fukuoka, *Appl. Catal. A Gen.*, 2011, **409-410**, 13–20.
- 24 T. Deng and H. Liu, *Green Chem.*, 2012, 116–124.
- 25 Y. Li, Y. Liao, X. Cao, T. Wang, L. Ma, J. Long, Q. Liu and Y. Xua, *Biomass and Bioenergy*, 2015, **74**, 148–161.
- 26 K. Li, M. Jiao, Y. Wang and Z. Wu, *Surf. Sci.*, 2013, **617**, 149–155.
- 27 J. Sarada Prasad, V. Dhand, V. Himabindu and Y. Anjaneyulu, *Int. J. Hydrogen Energy*, 2011, **36**, 11702–11711.
- 28 S. Esconjauregui, C. M. Whelan and K. Maex, *Carbon N. Y.*, 2009, **47**, 659–669.
- 29 A. M. Amin, E. Croiset and W. Epling, *Int. J. Hydrogen Energy*, 2011, **36**, 2904–2935.
- 30 M.-Y. Zheng, A.-Q. Wang, N. Ji, J.-F. Pang, X.-D. Wang and T. Zhang, *ChemSusChem*, 2010, **3**, 63–66.

- 31 B. Ravel and M. Newville, *J. Synchrotron Radiat.*, 2005, **12**, 537–541.
- 32 M. Lowell, S. Shields, J. E. Thomas, M. A. Thommes, *Characterization of Porous Solids and Powders: Surface Area, Pore Size and Density*, Kluwer Academic Publishers, 2004.
- 33 M. Thommes, K. Kaneko, A. V. Neimark, J. P. Olivier, F. Rodriguez-Reinoso, J. Rouquerol and K. S. W. Sing, *Pure Appl. Chem.*, 2015, **87**, 1051–1069.
- 34 G. F. Leal, L. A. Ramos, D. H. Barrett, A. A. S. Curvelo and C. B. Rodella, *Thermochim. Acta*, 2015, **616**, 9–13.
- 35 A. Y. Stakheev, I. C. Mashkovskii, O. P. Tkachenko, K. V. Klementiev, W. Grünert, G. N. Baeva and L. M. Kustov, *Russ. Chem. Bull.*, 2009, **58**, 280–283.
- 36 M. Bauer, R. Schoch, L. Shao, B. Zhang, A. Knop-Gericke, M. Willinger, R. Schlögl and D. Teschner, *J. Phys. Chem. C*, 2012, **116**, 22375–22385.
- 37 A. L. Bugaev, A. A. Guda, K. A. Lomachenko, V. V. Srabionyan, L. A. Bugaev, A. V. Soldatov, C. Lamberti, V. P. Dmitriev and J. A. van Bokhoven, *J. Phys. Chem. C*, 2014, **118**, 10416–10423.
- 38 J. a. McCaulley, *J. Phys. Chem.*, 1993, **97**, 10372–10379.
- 39 M. W. Tew, J. T. Miller and J. a. van Bokhoven, *J. Phys. Chem. C*, 2009, **113**, 15140–15147.
- 40 B. N. Nguyen, L. A. Adrio, T. Albrecht, A. J. P. White, M. A. Newton, M. Nachttegaal, S. J. A. Figueroa and K. K. (Mimi) Hii, *Dalt. Trans.*, 2015, **44**, 16586–16591.
- 41 A. Eyssler, P. Mandaliev, A. Winkler, P. Hug, O. Safonova, R. Figi, A. Weidenkaff and D. Ferri, *J. Phys. Chem. C*, 2010, **114**, 4584–4594.
- 42 a Löfberg, a Frennet and G. Leclercq, *J. Catal.*, 2000, **183**, 170–183.
- 43 C. Liang, F. Tian, Z. Li, Z. Feng, Z. Wei and C. Li, *Chem. Mater.*, 2003, **15**, 4846–4853.
- 44 F. H. Ribeiro, R. a. Dalla Betta, M. Boudart, J. E. Baumgartner and E. Iglesia, *J. Catal.*, 1991, **130**, 86–105.
- 45 F. H. Ribeiro, M. Boudart, R. A. D. Betta, R. A. Dalla Betta and E. Iglesia, *J. Catal.*, 1991, **513**, 498–513.
- 46 J. F. Wagner, C. D.; Riggs, W. M. ; Davis, L. E.; Moulder, *Handbook of X-ray Photoelectron Spectroscopy*, Perkin-Elmer Corporation, 1st edn., 1992.
- 47 J.-M. Giraudon, P. Devassine, J.-F. Lamonier, L. Delannoy, L. Leclercq and G. Leclercq, *J. Solid State Chem.*, 2000, **154**, 412–426.
- 48 S. Ahmed, A. Aitani, F. Rahman, A. Al-Dawood and F. Al-Muhaish, *Appl. Catal. A Gen.*, 2009, **359**, 1–24.
- 49 Y. Liu, C. Luo and H. Liu, *Angew. Chemie Int. Ed.*, 2012, **51**, 3249–3253.
- 50 N. Ji, T. Zhang, M. Zheng, A. Wang, H. Wang, X. Wang, Y. Shu, A. L. Stottlemyer and J. G. Chen, *Catal. Today*, 2009, **147**, 77–85.

- 51 Y. Cao, J. Wang, M. Kang and Y. Zhu, *J. Mol. Catal. A Chem.*, 2014, **381**, 46–53.
- 52 K. Fabičovicová, O. Malter, M. Lucas and P. Claus, *Green Chem.*, 2014, **16**, 3580–3588.
- 53 R. Sun, M. Zheng, J. Pang, X. Liu, J. Wang, X. Pan, A. Wang, X. Wang and T. Zhang, *ACS Catal.*, 2016, **6**, 191–201.
- 54 L. Zhou, J. Pang, A. Wang and T. Zhang, *Cuihua Xuebao/Chinese J. Catal.*, 2013, **34**, 2041–2046.
- 55 N. Yan, C. Zhao, C. Luo, P. J. Dyson, H. Liu and Y. Kou, *J. Am. Chem. Soc.*, 2006, **128**, 8714–8715.
- 56 P. Gallezot, *Chem. Soc. Rev.*, 2012, **41**, 1538–58.
- 57 M. Zheng, J. Pang, A. Wang and T. Zhang, *Chin. J. Catal.*, 2014, **35**, 602–613.
- 58 C. Li, M. Zheng, A. Wang and T. Zhang, *Energy Environ. Sci.*, 2012, **5**, 6383.
- 59 J. Pang, M. Zheng, A. Wang and T. Zhang, *Ind. Eng. Chem. Res.*, 2011, **50**, 6601–6608.
- 60 J. Pang, M. Zheng, R. Sun, L. Song, A. Wang, X. Wang and T. Zhang, *Bioresour. Technol.*, 2015, **175**, 424–429.

